

SURFACE ELECTRONS IN INVERTED LAYERS OF  $p$ -HgCdTe

SAMUEL E. SCHACHAM\* AND ELIEZER FINKMAN

\*NASA Lewis Research Center, Cleveland, OH 44135

Department of Electrical Engineering and Solid State Institute, Technion - Israel Institute of Technology, Haifa 32000, Israel.

\*This work was done while this author held a National Research Council - NASA Research Associateship.

## ABSTRACT

Anodic oxide passivation of  $p$ -type HgCdTe generates an inversion layer. Extremely high Hall mobility data for electrons in this layer indicated the presence of a two-dimensional electron gas. This is verified by use of the Shubnikov-de Haas effect from 1.45-4.15K. Data is extracted utilizing a numerical second derivative of DC measurement. Three sub-bands are detected. Their relative occupancies are in excellent agreement with theory and with experimental results obtained on anodic oxide as accumulation layers of  $n$ -type HgCdTe. The effective mass derived is comparable to expected.

## INTRODUCTION

The narrow-gap semiconductor HgCdTe is an important infrared detector material. Most photodiodes are implemented on  $p$ -type HgCdTe. The performance of these devices is heavily dependent on surface properties. Thus the selection of an appropriate passivation is crucial.

Anodic oxide forms an accumulation layer on  $n$ -type material. The two-dimensional sub-bands of this passivation have been thoroughly investigated in recent years. Findings obtained using various magnetoresistance measurements [1-7] are in good agreement with data obtained from other narrow-gap non-parabolic semiconductor systems, in particular on HgTe and HgTe/CdTe superlattices [8-10]. It has been shown both in theory [11,12], as well as experimentally [1,5,6] that narrow-gap non parabolic materials possess common features. One characteristic of accumulation and inversion layers on such materials is a large number of occupied sub-bands, as many as five in HgCdTe [5,6]. Ando [12] has shown that a large change in the band-gap energy has little effect on the relative occupancy of the various sub-bands.

In this work we report the use of the Shubnikov-de Haas (SdH) technique to measure the transport properties of electrons in an inversion layer on  $p$ -type  $\text{Hg}_{1-x}\text{Cd}_x\text{Te}$ . The inversion film was formed by generating an anodic oxide passivation to a low concentration  $p$ -type substrate,  $N_a - N_d \approx 8 \cdot 10^{14} \text{ cm}^{-3}$ , with composition ratio of  $x \approx 0.22$ . The low acceptor concentration enhanced the Hall data of the inversion layer. An extremely high Hall mobility, higher than measured for electrons in  $n$ -type material of similar composition, triggered our speculation that a 2-dimensional electron gas is present [13]. Since previous measurements concentrated on accumulation layers, it seemed intriguing to examine an inversion film, in particular since the theory of Takada et al. [11] was developed for the latter structure (see remark in [7]).

When a magnetic field is applied perpendicular to a surface layer, the translational motion is quantized into Landau levels. Sweep of the field reveals oscillations periodic with inverse magnetic field due to modulation of the density of states at the Fermi level as the Landau levels increase in energy with increasing field. When several sub-bands are occupied, these SdH measurements generate a waveform which is a superposition of the oscillations for each sub-band. The two-dimensionality of the structure can be verified by a vanishing signal as the sample is rotated by  $90^\circ$ .

Reprinted with permission of Materials Research Society.

## EXPERIMENTAL WORK

The measurement of DC magnetoresistance on HgCdTe frequently reveals little information. Seiler and Becker [14] introduced an AC technique where the magnetic field is modulated and phase sensitive detection is employed. The second derivative of the amplitude presents clear data of SdH oscillations [2,5,6,8,10]. An alternative method is using a metal-insulator-semiconductor (MIS) structure and modulating the gate voltage [1,7,15]. Since our experimental setup did not provide for modulation of the magnetic field and Hall bar samples were used, we had to develop appropriate numerical methods in order to extract the oscillatory data. Fourier analysis showed no oscillatory pattern following background subtraction. Instead numerical second derivative of the voltage with respect to the field combined with data smoothing was employed. These were obtained by fitting a small number of points to a second degree polynomial. This process eliminates the background and reveals the SdH oscillations.

Figure 1 shows such a plot of the second derivative versus an inverse magnetic field measured at 1.45 K. Several frequencies of oscillations can be observed, corresponding to various sub-band populations and their harmonics. In figure 2 we separated between these frequencies: trace (a), corresponds to 0.31-0.44 T, with a frequency of 3.75 T; trace (b), corresponds to 0.51-0.79 T, with a frequency of 9.7 T and a change of phase (beat) at 0.66 T; trace (c), corresponds to 1.01-1.16 T and shows superposition of the previous frequency with a 30.4 T waveform.

The effect of increasing temperature is presented in figure 3, in which trace 2c is repeated, this time at 4.15 K. There is an obvious decrease of the amplitude of the 30.4 T oscillation, while the reduction in the 9.7 T component is minimal.

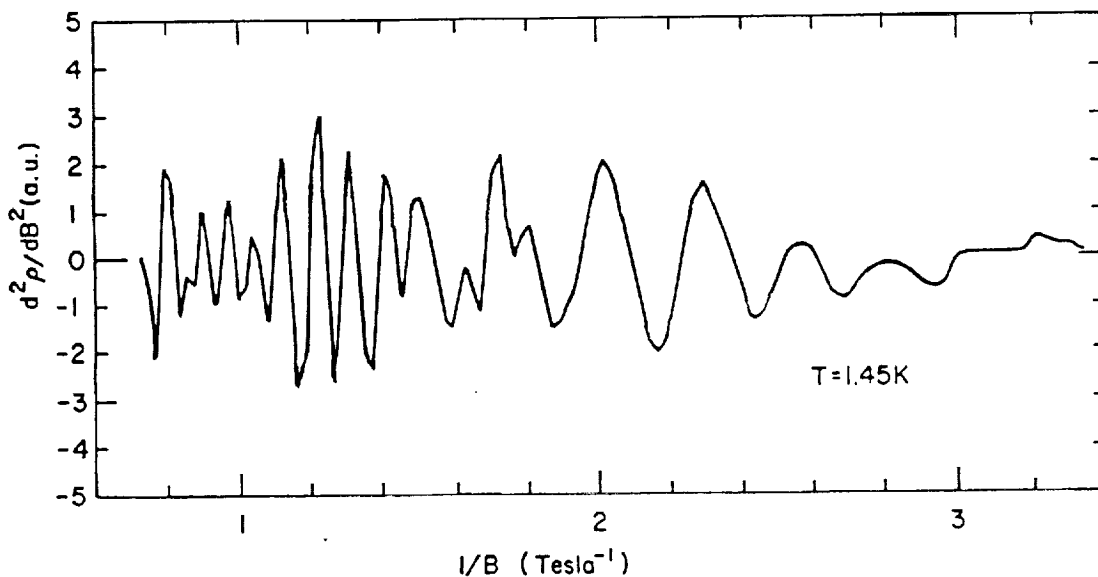


Fig. 1: Numerical second derivative of magnetoresistance measured at 1.45K, showing SdH oscillations of an anodic oxide inversion layer on  $p\text{-Hg}_{0.78}\text{Cd}_{0.22}\text{Te}$

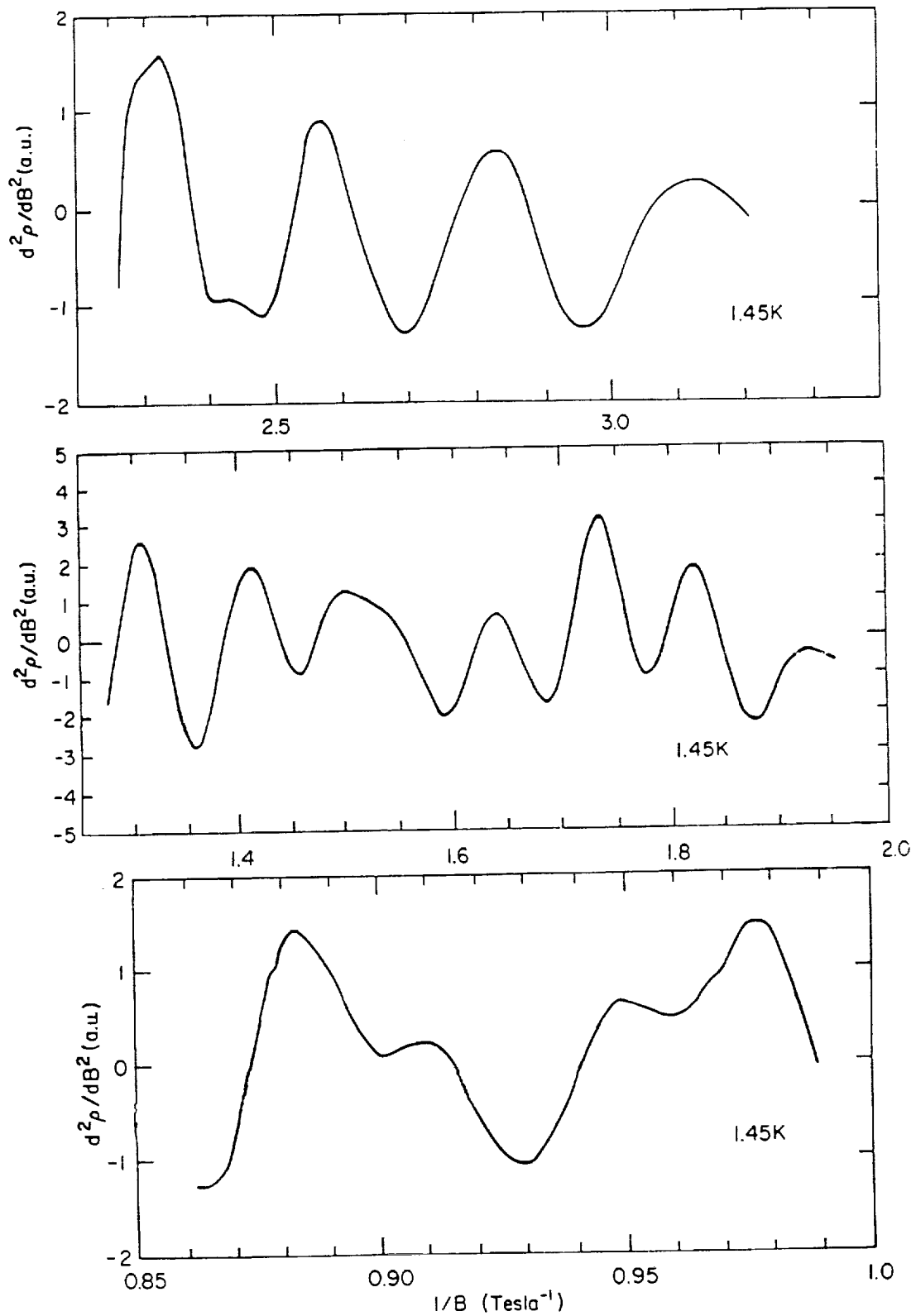


Fig. 2: High resolution data of Fig. 1, revealing 3 oscillation frequencies:  
 a. 0.31-0.44T,  $F = 3.75$ T.  
 b. 0.51-0.79T,  $F = 9.7$ T. Note the phase shift at  $\sim 1.52$   $1/T$ .  
 c. 1.01-1.16T, superposition of  $F = 9.7$ T and  $F = 30.4$ T.

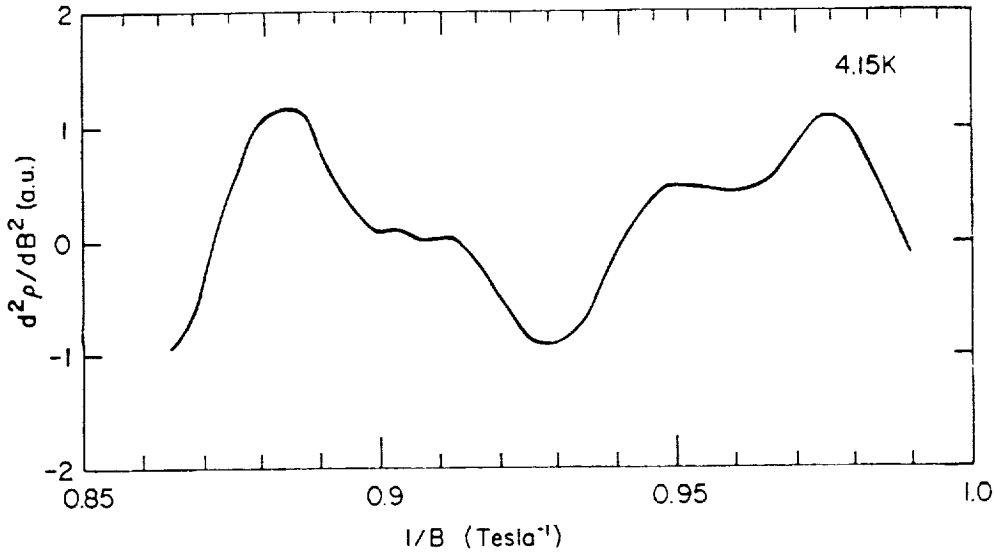


Fig. 3: Same as Fig. 2c, at 4.15, showing substantial decrease of 30.4T component, less of the 9.7 one.

#### ANALYSIS AND DISCUSSION

The change in the resistivity due to the magnetic field can be expressed as [16]

$$\frac{\Delta\rho}{\rho_0} \propto \sum_n \sum_M T \left[ \frac{M \cdot m_r^n}{B} \right]^{1/2} \frac{\exp(-\beta M T_D^n m_r^n / B)}{\sinh(\beta M T m_r^n / B)} \cdot \cos \left[ \frac{2\pi M F^n}{B} + \phi^n \right] \quad (1)$$

where  $T$  = temperature,  $B$  = magnetic field,  $F$  = oscillation frequency,  $\phi$  = phase,  $T_D$  = Dingle temperature,  $m_r$  = effective mass ratio ( $m^*/m_0$ ), and  $\beta = 2\pi^2 k_B m_0 / H B e = 14.7$  T/K. The summation on  $M$  is over the harmonic frequencies of a given sub-band  $n$ . In order to obtain the occupancy of the various sub-bands, the Fourier transform of the data was obtained using an FFT. Figure 4 shows a transform of the second derivative taken at 4.15 K. Similar spectra were obtained for all other measured temperatures. These results highly resemble the data of Beck and Anderson (Fig. 2, Ref. 7), obtained for an accumulation layer. In addition to the three main frequencies, corresponding to three occupied sub-bands, one can easily observe the second and third harmonics of the 3.75 T line (with the third harmonic more intense than the second).

The effective mass of electrons in the various sub-bands can be derived from the reduction in amplitude with increasing temperatures. This dependence can be summarized as  $\chi/\sinh \chi$ , where  $\chi = \beta T m_r / B$ . Unfortunately due to the very small effective mass in HgCdTe and due to the superposition of the various lines, it is hard to obtain precise data in the limited temperature range employed. Figure 5 shows a fit for the amplitude of a peak at 1.05 T (0.95 1/T) which corresponds to the first sub-band, with the largest effective mass. The fitted value is  $m^* = 0.033 m_0$ . The convex shape of the curve indicates that the argument of the hyperbolic function is indeed small, thus replacing the hyperbolic sine with an exponential function should be done with extreme caution! [9]. The data is summarized in Table I. The uncertainty in the value of the effective masses is large. Moreover, since the ratio of  $x$  to its hyperbolic sine approaches rapidly 1 as  $x$  approaches 0, the very small effective masses of the second and third subbands renders a ratio which is almost temperature independent, causing a further increase in uncertainty in determination of these values. The accuracy of the derivation may be improved by either a deconvolution of the various frequency components of the waveform, or a simulation this pattern.

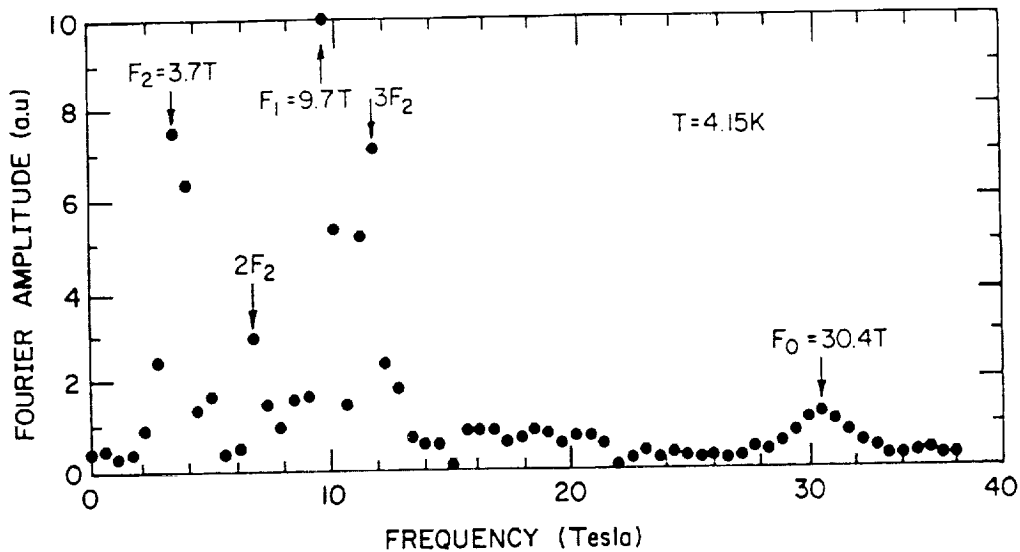


Fig. 4: Fourier transform of SdH oscillations. Clear peaks of 3 fundamental frequencies, due to 3 sub-bands, and harmonics of  $F = 3.75T$ .

The sub-band occupancy is given by  $N_s^n = \frac{2e}{h} \cdot F^n$ . Summing up the concentration of the first three sub-bands, and adding 4% for the higher ones [5], we came up with the ratio of the sub-bands occupancy to total surface concentration  $N_s^T$ , presented in Table I.

Table I

$n$	$F^n(T)$	$N_s^n(cm^{-2})$	$N_s^n/N_s^T$	$m_r^n$
1	30.4	$1.47 \cdot 10^{12}$	0.693	$0.033 \pm 0.008$
2	9.7	$4.69 \cdot 10^{11}$	0.221	$0.018 \pm 0.007$
3	3.75	$1.81 \cdot 10^{11}$	0.0855	$0.011 \pm 0.005$

The concentration ratios are in excellent agreement with the theory in [12], the results of Beck and Anderson [7] and the various Singleton, Nicholas and Nasir investigations [1-6]. Taking into consideration the composition ratio ( $x = 0.22$ ), our results indeed fit perfectly with a slight difference between those of  $x = 0.2$  and  $x = 0.3$  [2]. The discrepancy between these data and that of Zhao et al. [1] was recently explained [5].

The effective masses obtained are on the lower edge of the theory [11] and experimental results [6,7]. However, the large uncertainty in present values necessitates further investigation before any conclusions can be drawn.

The two-dimensionality of the data was verified by rotating the sample by  $90^\circ$ . The numerical analysis renders noise with amplitudes one-order of magnitude smaller than the SdH oscillations, for all temperatures tested. No peaks are present in the Fourier transform.

A change of phase, such as we observed at about 0.66 T, has been previously reported for SdH data on various materials, including HgTe films [8]. The last one was observed only at  $\sim 1.9$  K, and was attributed to strain-effects, rather than to inversion asymmetry, since it was observed at low electron concentration. In this work it is also possible that the beat is a result of the superposition of the two frequencies at 9.7 T (second sub-band) and at 11 T (third harmonic third sub-band).

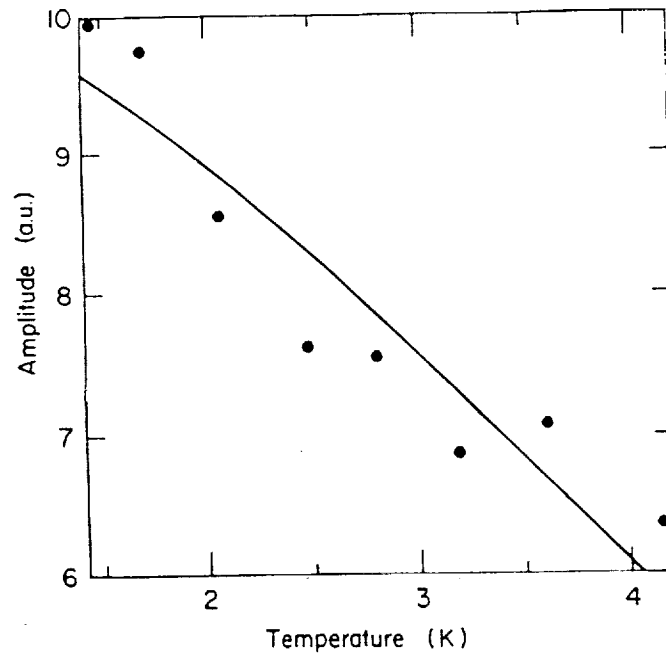


Fig. 5: Measured temperature dependence of peak at 1.05T.  
Effective mass derived from theoretical fit  $m^* = 0.33m_0$ .

## CONCLUSIONS

The SdH experimental technique performed on an inversion layer, generated by anodic oxidation of a *p*-HgCdTe, proves the existence of a 2DEG and renders data on three sub-bands. The calculated relative occupancies of these sub-bands agree extremely well with theory and experimental results obtained from accumulation layers on *n*-type materials. The analysis should be extended to achieve better accuracies of the effective mass by both measurements at higher temperatures and by mathematical simulation of the data. This also may render scattering times. Experimental work at higher magnetic fields may reveal additional structures.

The numerical analysis performance in this work has proven that it is possible to compensate for limitations in experimental facilities by appropriate mathematical tools.

## REFERENCES

1. W. Zhao, F. Koch, J. Ziegler and H. Maier, Phys. Rev. B 31, 2416 (1985).
2. J. Singleton, R.J. Nicholas, F. Nasir and C.K. Sarkar, J. Phys. C 19, 35 (1986).
3. J. Singleton, F. Nasir and R.J. Nicholas, in Optical Properties of Narrow-Gap Low-Dimensional Structures, Vol. 152 in NATO ASI Series B, edited by C.M.S. Torres, J.C. Portal, J.C. Maan and R.A. Stradling (Plenum, New York, 1987), p. 195.
4. J. Singleton, F. Nasir and R.J. Nicholas, Proc. SPIE 659, 99 (1986).
5. F. Nasir, J. Singleton and R.J. Nicholas, Semicond. Sci. Technol. 3, 654 (1988).
6. R.J. Nicholas, F. Nasir and J. Singleton, J. Cryst. Growth 86, 656 (1988).
7. W.A. Beck and J.R. Anderson, J. Cryst. Growth 72, 437 (1985).

8. R.J. Justice, D.G. Leider, W. Zawadzki, R.J. Koestner, M.G. Goodwin and M.A. Kinch, *J. Vac. Sci. Technol. A* 6, 2779 (1988).
9. L. Ghenim, R.G. Mani and J.R. Anderson, *Phys. Rev. B* 39, 1419 (1989).
10. D.G. Seiler, G.B. Ward, R.J. Justice, R.J. Koestner, M.W. Goodwin, M.A. Kinch and J.R. Meyer, *J. Appl. Phys.* 66, 303 (1989).
11. Y. Takada, K. Arai, N. Uchimura and Y. Vemura, *J. Phys. Soc. Jpn.* 49, 1851 (1980).
12. T. Ando, *J. Phys. Soc. Jpn.* 54, 2676 (1985).
13. S.E. Schacham and E. Finkman, to be published in *Opt. Eng.*
14. D.G. Seiler and W.M. Becker, *Phys. Rev.* 183, 784 (1969).
15. J.C. Thuillier and F. Bazenet, *J. Vacuum Sci. Technol.* 16, 1417 (1979).
16. E.N. Adams and T.D. Holstein, *J. Phys. Chem. Solids* 10, 254 (1959).

# PLASMA-DEPOSITED AMORPHOUS HYDROGENATED CARBON FILMS AND THEIR TRIBOLOGICAL PROPERTIES

K. Miyoshi, J.J. Pouch and S.A. Alterovitz

National Aeronautics and Space Administration  
Lewis Research Center, Cleveland, OH 44135, USA

## ABSTRACT

Recent work on the properties of "diamondlike" carbon films and their dependence on preparation conditions are reviewed. The results of the study indicate that plasma deposition enables one to deposit a variety of amorphous hydrogenated carbon (a-C:H) films exhibiting more diamondlike behavior to more graphitic behavior. The plasma-deposited a-C:H can be effectively used as hard, wear-resistant, and protective lubricating films on ceramic materials such as  $\text{Si}_3\text{N}_4$  under a variety of environmental conditions such as moist air, dry nitrogen, and vacuum.

## INTRODUCTION

Carbon films exhibiting unique properties can be formed on different substrates by ion-beam deposition, ion-beam sputtering, and plasma deposition of gaseous hydrocarbons [1 to 8]. The properties are sensitive to the deposition conditions. These resulting films can exhibit high electrical resistivity, semitransparency, mechanical hardness, and chemical inertness. The carbon films show promise as wear-resistant, hard solid lubricating coatings for mechanical systems such as bearings and optical components. In addition, carbon films are useful as gate dielectrics and passivating layers in semiconductor device processing, insulators for metal-insulator-metal fabrication, and masks for nanometer lithography [9 to 11].

This chapter is principally concerned with the chemical, physical, and tribological characteristics of amorphous hydrogenated carbon (a-C:H) films grown on different substrates ( $\text{Si}_3\text{N}_4$ , GaAs, InP, Si, and fused silica) by means of plasma chemical vapor deposition at 30 kHz. The influence of growth conditions on the chemical and physical properties of these films was studied by Auger electron spectroscopy (AES), secondary ion mass spectroscopy (SIMS), x-ray photoelectron spectroscopy (XPS), ellipsometry, and  $\text{N}^{15}$  nuclear reaction techniques. The nuclear reaction techniques provide the hydrogen concentration information. These analysis techniques and procedures are described in references 12 to 18. Tribological studies have also been conducted with the a-C:H films to better understand those chemical and physical properties of the films that will affect their tribological behavior when in contact with a ceramic material. The friction, wear, and lubricating behavior of the a-C:H films were examined with flat specimens (composed of an a-C:H film and  $\text{Si}_3\text{N}_4$  substrate) in contact with  $\text{Si}_3\text{N}_4$  riders in two processes. The first was done in dry nitrogen gas in moist air to determine the environmental effects on friction and resistance to wear of the a-C:H films. The second was done in an ultrahigh vacuum system to determine the effect of temperature on adhesion and friction of a-C:H films.

# AMORPHOUS HYDROGENATED CARBON (a-C:H) FILMS

## Plasma Deposition

Amorphous hydrogenated carbon films were formed on the different substrates from the 30 kHz ac glow discharge by using a planar plasma reactor [12 to 18]. All substrate materials were first cleaned in acetone and ethanol baths and then rinsed in deionized water. The substrates were placed on the ground anode of the parallel plate reactor in the chamber; the upper electrode was capacitively coupled to the 30 kHz power source. The background pressure was typically 2.7 Pa (20 mtorr). The gas sources were  $\text{CH}_4$  and  $\text{C}_4\text{H}_{10}$  (methane and butane, 99.97 percent pure). The deposition gas ( $\text{CH}_4$  or  $\text{C}_4\text{H}_{10}$ ) was used to flush the system three times prior to each run. The chamber pressure was controlled by the input gas flow rate and pumping speed. The power density and flow rate settings covered the ranges  $0.4$  to  $5 \text{ kW m}^{-2}$  (25 to 300 W) and  $3$  to  $9 \times 10^{-5} \text{ m}^3 \text{ min}^{-1}$  (30 to 90 SCCM), respectively. The initial substrate temperature was  $25^\circ\text{C}$ , and it increased a few degrees during each deposition.

The film growth rate varied monotonically with deposition power. Figure 1 illustrates the typical dependence of growth rate on deposition power. The specimens are a-C:H films grown on InP substrates using a  $\text{CH}_4$  flow rate of 70 SCCM. This growth rate increases from 5 to  $27 \text{ nm min}^{-1}$  as the power increases from 25 to 300 W.

## Film Characteristics

The AES and XPS measurements indicated that the a-C:H films contained only carbon; no other element was observed to the detection limits (0.1 at. %) of the instrument [12 and 13]. Figure 2 shows a typical AES profile of a-C:H films on the InP and GaAs. Oxygen was not present in the films, but there was a small percentage of oxygen at the carbon-InP interface. This suggests that the  $\text{CH}_4$  (methane) plasma removes all of the native oxides from the GaAs surfaces and most of it from the InP surfaces.

Relative counts of hydrocarbon ions sputtered from a-C:H films deposited on the InP substrate were determined by means of SIMS depth-profiling studies performed with 3 keV  $\text{Ar}^+$  ions [12]. In figure 3(a) the distribution of ion counts is plotted as a function of mass-to-charge ratio for various deposition conditions using a  $\text{C}_4\text{H}_{10}$  plasma. The predominant ion is  $\text{CH}^+$ ; it is interesting that a higher  $\text{CH}^+$  level is obtained from films produced at the higher power densities. Additional ions are presented in figure 3(a):  $\text{CH}_2^+$ ,  $\text{CH}_3^+$ ,  $\text{C}_2\text{H}^+$ ,  $\text{C}_2\text{H}_2^+$ , and  $\text{C}_2\text{H}_3^+$ .

The ion distributions extracted from a-C:H films prepared by a  $\text{CH}_4$  (methane) discharge are shown in figure 3(b). Evidently,  $\text{CH}^+$  has a higher probability of being sputtered from each film. At 50 SCCM (32.7 Pa), more  $\text{CH}^+$  is generated from the a-C:H deposit made at  $2.45 \text{ kW m}^{-2}$ . In addition, some of the films obtained from the  $\text{C}_4\text{H}_{10}$  discharge (fig. 3(a)) have higher amounts of incorporated  $\text{C}_2\text{H}_3$  relative to the  $\text{CH}_4$ -derived films (fig. 3(b)). Figure 3 indicates that the lowest populations are associated with  $\text{CH}_3^+$ . The ion distributions thus reflect some of the bonding arrangements that result from the interaction of the plasma radicals with the growing film [19 to 21].

A SIMS depth profile (3 keV  $\text{Ar}^+$  ions) of carbon deposited onto GaAs using  $\text{C}_4\text{H}_{10}$  is presented in figure 4. The  $\text{CH}_x^+$  ( $x = 0, 1, 2, 3$ ) distributions are uniform in the bulk of the film, and they drop to lower levels in the vicinity

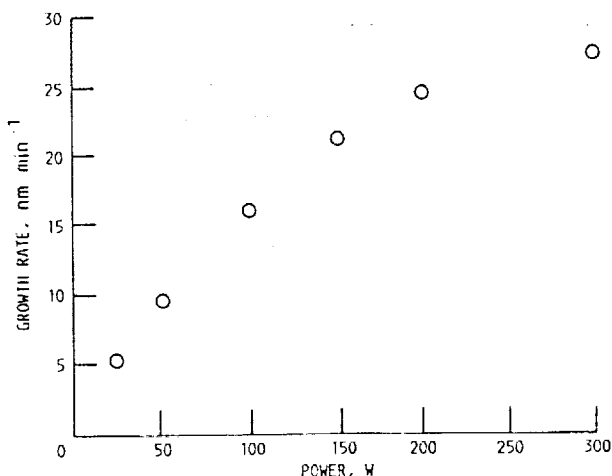


Figure 1.—Growth rate of hydrogenated carbon on *n*-InP as function of deposition power.

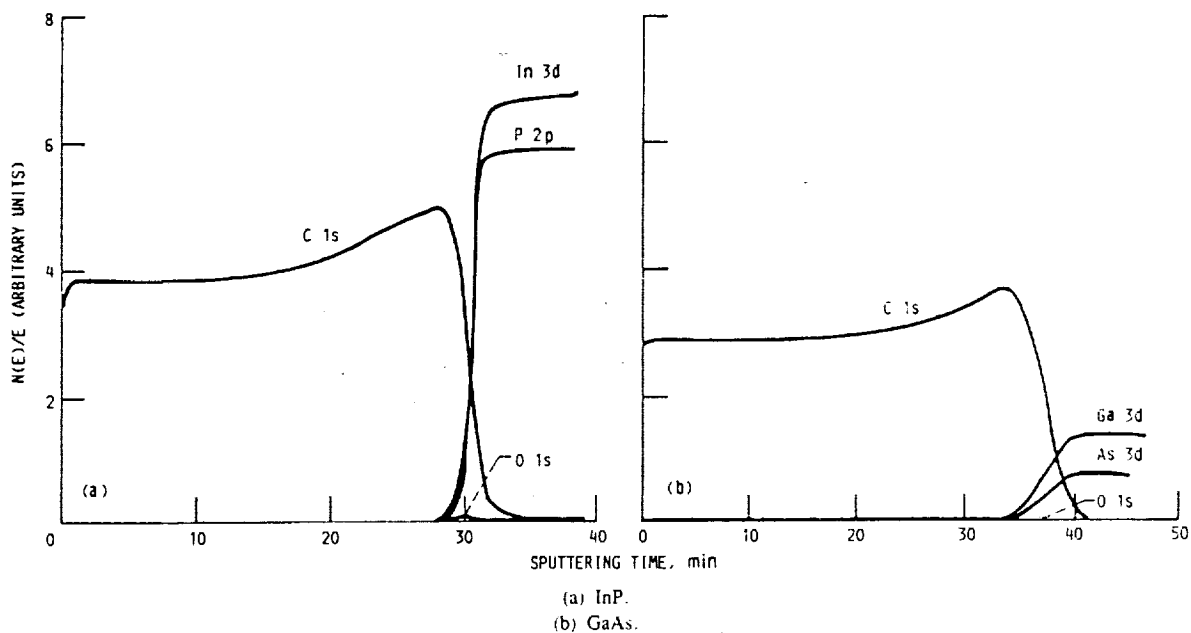


Figure 2.—Auger electron spectroscopy (AES) profiles of carbon films on InP and GaAs, using 25 mA 3 keV Ar<sup>+</sup> ions.

of the carbon-GaAs interface. Moreover, figure 4 shows oxygen to be present throughout the film. This determination cannot be made with the less-sensitive AES technique. It is apparent that Ga<sup>+</sup> and As<sup>+</sup> are readily detected as the carbon film is sputtered away.

The argon ion etching rate of the a-C:H films is shown as a function of deposition power in figure 5(a). An inverse relationship between argon ion etching rate and deposition power is observed. The etching rate drops from 80 to 50 nm min<sup>-1</sup> when the deposition power is increased from 25 to 300 W. This suggests that films grown at higher powers are denser than those grown at lower powers. Figure 5(b) shows the nuclear reaction analyses data. The hydrogen concentration in the carbon film decreases slightly with increasing power. The hydrogen concentrations are in the 7.2 to 7.7 × 10<sup>22</sup> cm<sup>-3</sup> range, which gives an approximate value of 0.8 for *x* in the formula CH<sub>*x*</sub>.

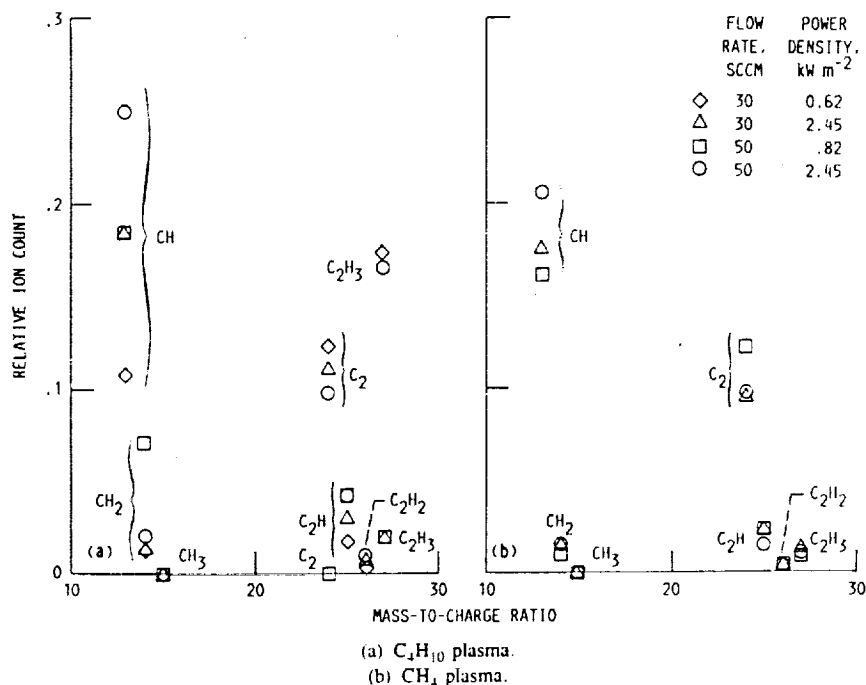


Figure 3.—Relative ion count as function of mass-to-charge ratio for carbon deposited onto InP using C<sub>4</sub>H<sub>10</sub> and CH<sub>4</sub> plasmas.

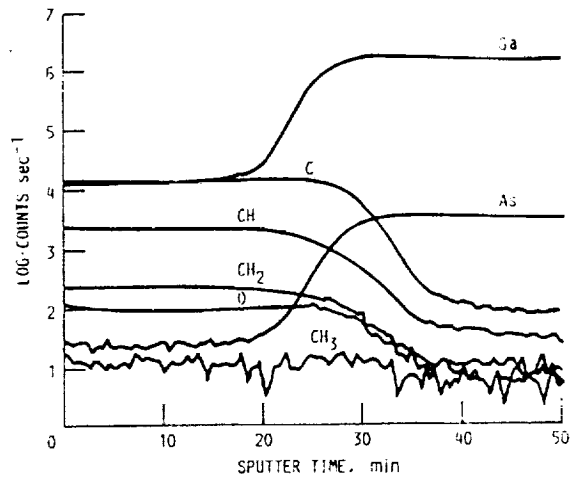


Figure 4.—Secondary ion mass spectroscopy (SIMS) depth profile of carbon on GaAs using 3 keV Ar<sup>+</sup> ion bombardment.

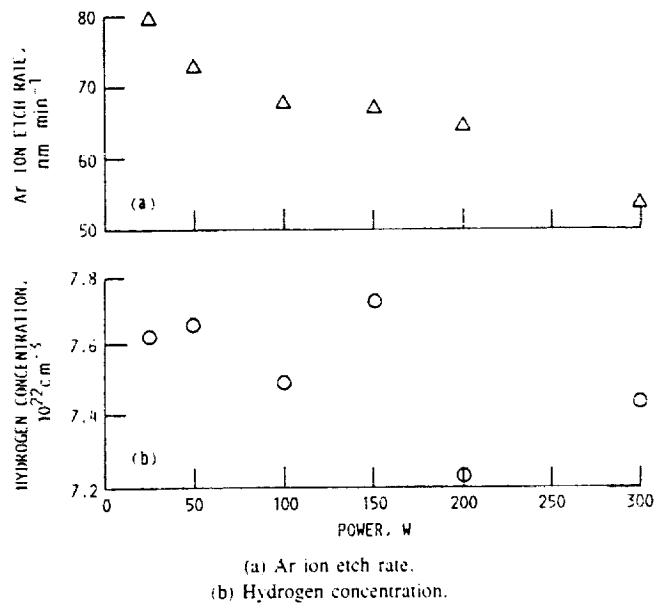


Figure 5.—Ar ion etching rate and hydrogen concentration as function of deposition power for carbon film grown on *n*-InP.

TABLE 1.—COMPOSITION AND PROPERTIES OF HOT-PRESSED SILICON NITRIDE

Nominal composition, wt %	92 Si <sub>3</sub> N <sub>4</sub> -4MgO-4Y <sub>2</sub> O <sub>3</sub>
Structural phase	β-Phase
Density, g cm <sup>-3</sup>	3.27
Vickers hardness, GPa	16.1
Three-point bending strength, MPa	980
Fracture toughness, MN m <sup>-3/2</sup>	9.4
Young's modulus, 10 <sup>4</sup> kg mm <sup>-2</sup>	2.9
Poisson's ratio	0.27
Compressive strength, kg mm <sup>-2</sup>	330
Thermal expansion coefficient, 10 <sup>-6</sup> °C <sup>-1</sup>	3.6

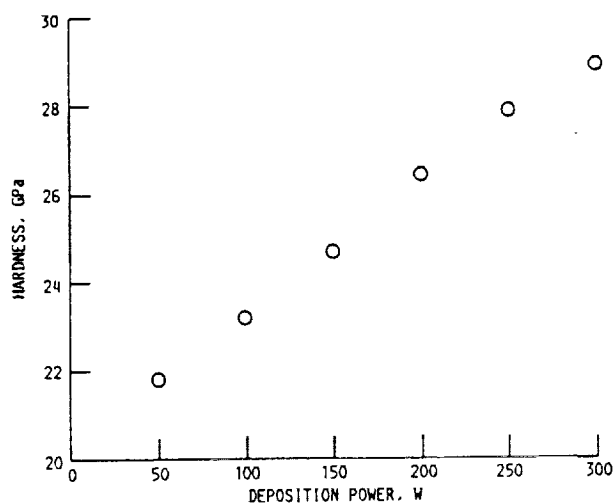


Figure 6.—Vickers hardness as function of deposition power for a-C:H film deposited on  $\text{Si}_3\text{N}_4$  (hardness measuring load, 0.25 N; hardness of  $\text{Si}_3\text{N}_4$  substrate, 17.1 GPa).

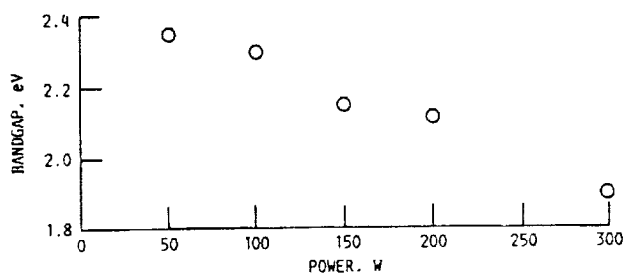


Figure 7.—Optical bandgap as function of deposition power for carbon film grown on n-InP.

The microhardness data measured for the carbon films on  $\text{Si}_3\text{N}_4$  substrate (table I) at various deposition powers are presented in figure 6. The microhardness increases as the power increases. Thus it appears that a decrease in hydrogen concentration is accompanied by an increase in film density and/or c-c bondings, and in hardness.

The optical energy gap is shown as a function of the deposition power in figure 7. A decrease in the optical energy gap is clearly observed with increasing power.

At this stage, we will compare our results with conjecture forwarded by S. Kaplan et al. [22]. They claim that since double-bond hydrogenation is an exothermic process, "graphitic" behavior is favored over tetrahedral bonding in higher energy growth environments. They show evidence of this assumption by comparing a-C:H films made by five different experimental configurations. As a-C:H properties are dependent quite strongly on the many variables encountered in different preparation conditions, it seems that a better test of this assumption is in order. In addition, their results show a rather striking feature: a-C:H films exhibiting more "diamondlike" behavior (i.e., larger bandgap and more tetrahedral bonding) show a steep decrease in their hardness as compared with the more "graphitic" films. Our results confirm this model, including the hardness measurements. The higher the plasma deposition power, the more  $sp^2$  versus  $sp^3$  bonds are made, giving a more "graphitic" film, with smaller bandgap (fig. 7) and higher density and hardness (figs. 5 and 6, respectively).

### TRIBOLOGICAL PROPERTIES

In the preceding section there have been indications that a-C:H films have diamondlike behavior in lower energy growth environments as compared with the more graphitic behavior in higher energy growth environments. Therefore, the objective of this section is to compare the tribological properties of a-C:H films made by different deposition powers.

Sliding friction and wear experiments were conducted with a-C:H films deposited on  $\text{Si}_3\text{N}_4$  flats in contact with hemispherical  $\text{Si}_3\text{N}_4$  riders (1.6 mm in radius). The a-C:H films on the  $\text{Si}_3\text{N}_4$  flat substrates were approximately  $0.06 \mu\text{m}$ . The  $\text{Si}_3\text{N}_4$  used for flat substrates and hemispherical riders was hot pressed, and its composition and some of its properties are presented in table I. Two types of sliding friction experiments were conducted with the a-C:H films [23 to 25]. The first type was conducted in nitrogen and laboratory air atmospheres with a load of 1 N (Hertzian contact pressure, 910 MPa) and at a sliding velocity of  $8 \text{ mm min}^{-1}$  at room temperature. The specimen rider was made to traverse on the surface of a-C:H film. The motion was reciprocal. The a-C:H films were subjected to multipass sliding by the  $\text{Si}_3\text{N}_4$  riders. The second type was conducted in ultrahigh vacuum ( $10^{-8}$  to  $10^{-9}$  torr) with loads up to 1.7 N (Hertzian contact pressure, 1.5 GPa) and at a sliding velocity of  $3 \text{ mm min}^{-1}$  at temperatures up to  $700^\circ\text{C}$ . In this case, the a-C:H films were subjected to single-pass sliding by the  $\text{Si}_3\text{N}_4$  riders.

### Environmental Effects on Friction and Wear

Environment significantly changes the friction and wear behavior of solid materials. Friction and wear of a-C:H films are consistent with this generality and depend on water vapor [1 and 26 to 28].

Figure 8 presents typical plots of the coefficient of friction for plasma-deposited a-C:H films at low (50 W) and high (250 W) deposition power as a function of the number of repeated passes in dry nitrogen and humid air environments. The values of coefficient of friction given are typical, but the trends with number of passes are quite reproducible. With the 50-W plasma-deposited a-C:H films, the coefficient of friction was generally found to increase.

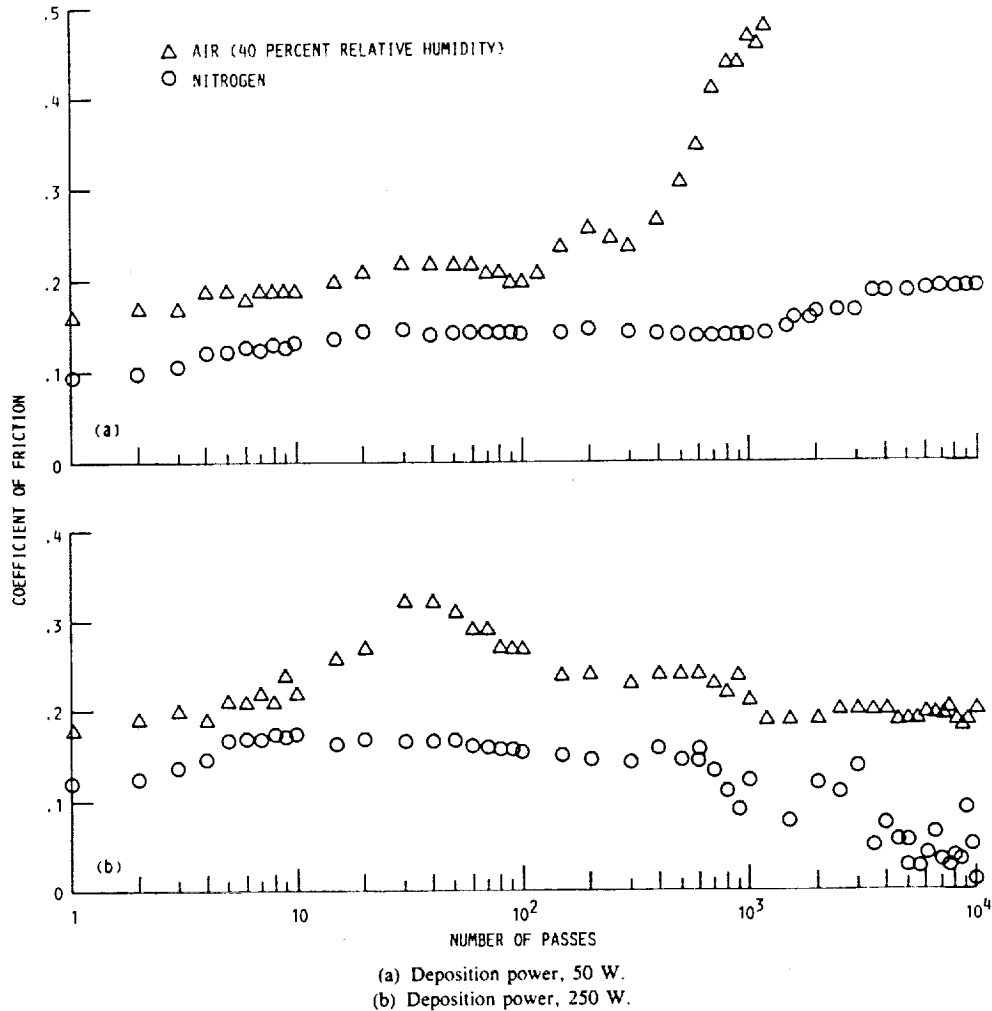


Figure 8.—Average coefficient of friction as function of number of passes of  $\text{Si}_3\text{N}_4$  rider across a-C:H film surface in laboratory air and dry nitrogen at deposition powers of 50 and 250 W.

as shown in figure 8(a). This increase, however, was small in a dry nitrogen environment even after it had been in contact with the rider for about 10 000 passes. On the other hand, in humid laboratory air a significant increase in the coefficient of friction occurred at about 500 passes and increased sharply to 1000 passes. The sliding action caused breakthrough of the film and removed it from the sliding contact area at about 1000 passes. Note that among the a-C:H films deposited at various deposition powers (50 to 300 W), the film deposited at 50 W has the lowest initial coefficient of friction (0.08 to 0.09) in the dry nitrogen environment. The value of the coefficient of friction was similar to that of a hemispherical diamond pin (radius, 0.2 mm) in sliding contact with a  $\text{Si}_3\text{N}_4$  flat. The friction of the diamond was low (0.05 to 0.1) in dry nitrogen. It is well known that diamond has a low coefficient of friction in contact with various types of materials [29].

With the 250-W plasma-deposited a-C:H films (fig. 8(b)), although the coefficient of friction increased with increasing number of passes for about 10 passes in the dry nitrogen environment, it generally decreased in the range 10 to 10 000 passes.

At 600 to 700 passes, the coefficients of friction became very erratic and variable, as presented in figure 8(b). Optical microscopic examination indicated that some wear debris particles formed in the front region of the rider and on the wear track of the a-C:H film. Thus the wear particles so produced were caught up in the sliding mechanism and affected the coefficient of friction.

At 1000 passes and above, the coefficient of friction became low, but still variable (0.01 to 0.1). At this range the coefficients of friction for the 250-W plasma-deposited film were lower than those for the film deposited at 50 W.

In a humid air environment, the coefficients of friction for the 250-W plasma-deposited a-C:H film were higher as compared with those in dry nitrogen by a factor of 1.5 to 3 up to 10 000 passes. The film, however, did not wear off from the substrate even in the humid air environment.

Thus, water vapor greatly increases friction and reduces the wear life of plasma-deposited a-C:H film at low deposition powers. In general, a-C:H films deposited with lower deposition powers were more susceptible to water vapor, when compared with the films deposited with higher deposition power. Particularly, the deposition power greatly affects the wear life of the films in a humid air environment. The greater the deposition power (the more graphitic the film), the greater the wear life in humid air.

### Annealing Effects on Friction and Wear

Thermal annealing significantly affects the properties of a-C:H films. For example, an abrupt decrease of the optical bandgap has been observed for the thermal annealing process [14].

Figure 9 presents the optical bandgap of the a-C:H films deposited on the quartz substrates by using 150-W, 70-SCCM-flow-rate  $\text{CH}_4$  plasma as a function of annealing time at 400 and 600 °C. The thermal processing of the films was accomplished in nitrogen gas with tungsten halogen light. The main part of the reduction in the optical bandgap is obtained at short annealing time. This fact can also be deduced by the result obtained by laser annealing [30].

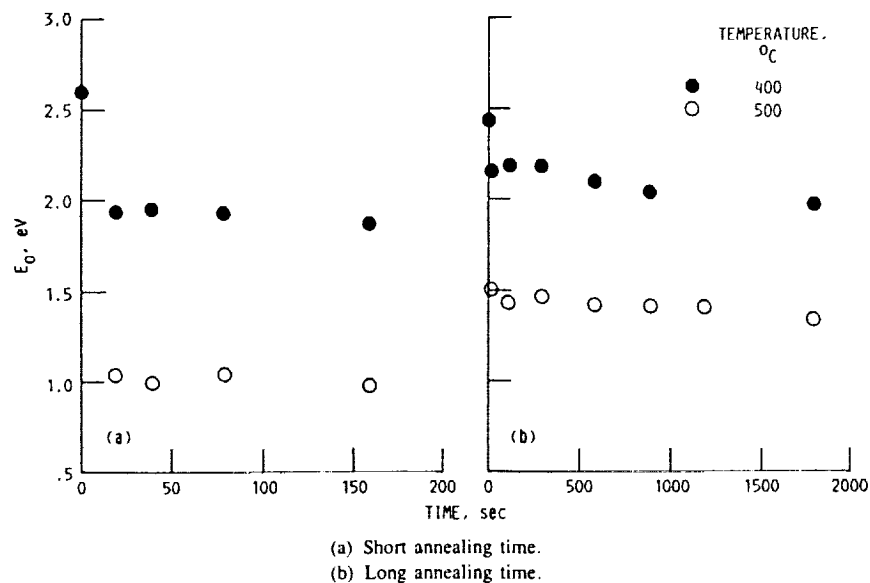


Figure 9.—Optical energy gap  $E_g$  as function of annealing time for a-C:H films on quartz annealed at two temperatures.

when processing time is much shorter than that reported here. The mechanism involved should be a two-step process. There is known to be a two-stage pyrolysis of organic material into graphite [31] for temperatures in this range, namely carbonization and polymerization. The carbonization stage includes loss of volatile matter, which we identify with hydrogen loss in this case [1]. This stage occurs in the temperature range 400 to 600 °C in a-C:H. The polymerization stage includes the formation of graphitic crystallites or sheets. If we assume that the polymerization is a diffusion-dependent process with a relatively long time constant (on the order of  $10^3$  sec), then we can deduce that the two processes of carbonization and polymerization occur simultaneously in our a-C:H films. The abrupt decrease of the bandgap versus time at very short processing time is due to the hydrogen loss, while the subsequent decrease in optical bandgap is due to an increase in cluster size [31].

Further, absorption in the UV-visible range was measured with a-C:H films on quartz substrates [14]. The absorbance-versus-wavelength plot at 600 °C shows a decrease in peak height and a shift in the peak position. The shift indicates changes in the carbon bonding. The decrease in peak height is attributed mostly to loss of material in this case.

Thermal annealing also changes the friction and wear characteristics of a-C:H films. Figure 10 presents the friction data for annealed a-C:H films in sliding contact with  $\text{Si}_3\text{N}_4$  riders in dry nitrogen and humid air environments. The

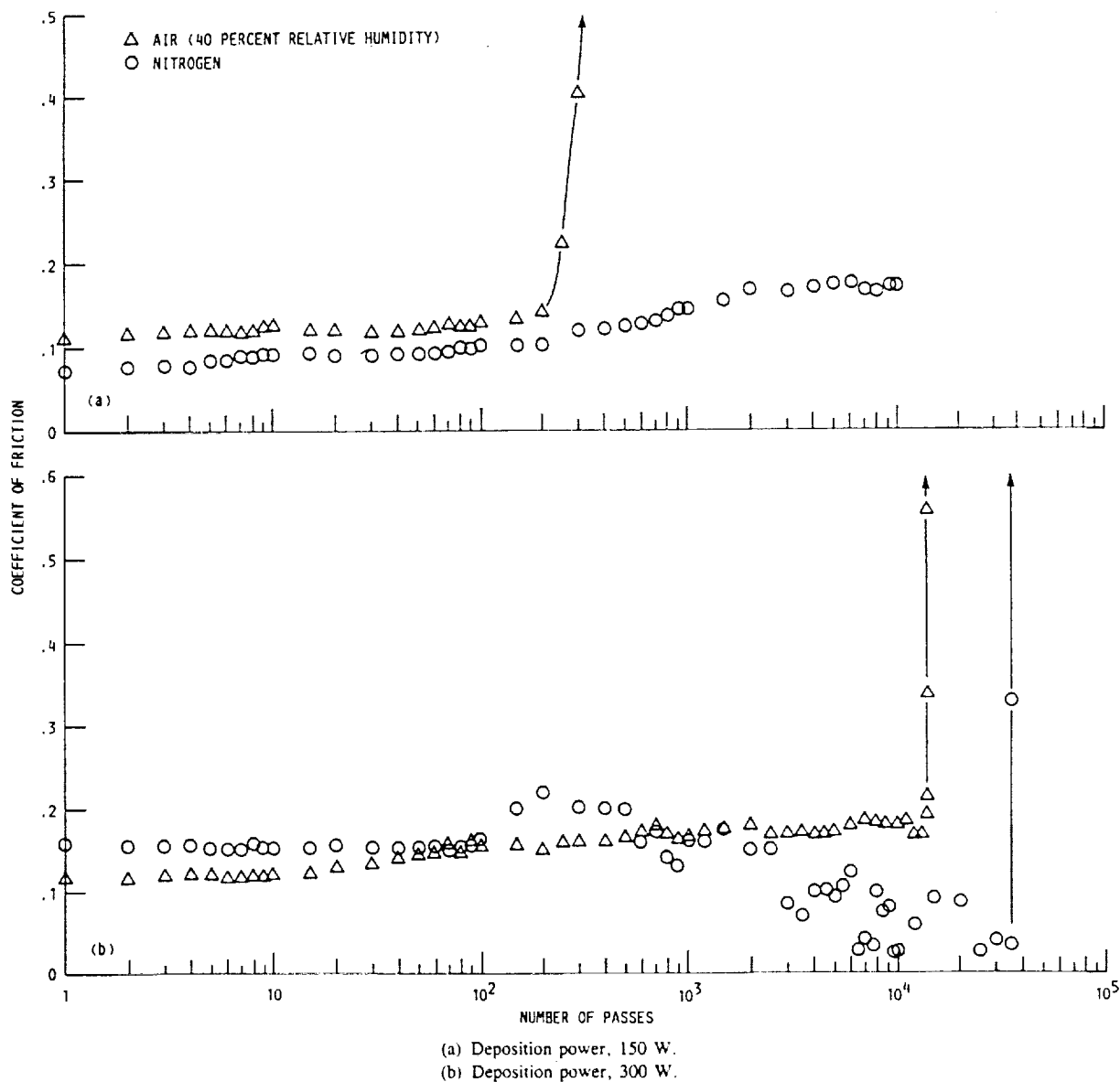


Figure 10.—Average coefficient of friction as function of number of passes of  $\text{Si}_3\text{N}_4$  rider across a-C:H film surface in laboratory air and in dry nitrogen, after annealing a-C:H in vacuum at 700 °C, at deposition powers of 150 and 300 W.

annealing of the a-C:H films deposited on the  $\text{Si}_3\text{N}_4$  substrates was accomplished at 700 °C in ultrahigh vacuum ( $10^{-8}$  to  $10^{-9}$  torr).

Both in dry nitrogen and in humid air, the initial coefficients of friction for the annealed film deposited at 150 W (fig. 10(a)) were reduced by about a factor of 2 as compared with those for as-deposited film. The annealed film did not wear off from the substrate in dry nitrogen even after it had been in contact with the rider for about 10 000 passes, while in humid nitrogen it wore off at 300 passes and had shorter wear life.

With the a-C:H deposited at 300 W (fig. 10(b)), the results show an interesting feature: the annealed film exhibited more graphitic behavior; that is, at up to 100 passes the initial coefficients of friction in humid air were lower than those obtained in dry nitrogen. This is contrary to the results obtained from the as-deposited a-C:H films (e.g., fig. 10) and the annealed film at 150 W power (fig. 10(a)). Further, in the humid air environment the coefficients of friction were reduced by about a factor of 2 as compared with the as-deposited film. The generally accepted theory (that graphite lubricates because of adsorbed water or gaseous films) seems capable of explaining these results [32 and 33]: namely, the a-C:H film deposited at 300 W is believed to be more graphitic than the films deposited at lower power. Moreover, the annealing of the film gives a more graphitic film. Effective lubrication is possible with the very graphitic film provided both by the high-power plasma deposition and by the annealing process when an adsorbed water vapor film is present. Thus, the annealed a-C:H film deposited at 300 W has very graphitic friction behavior.

### Temperature Effects on Adhesion and Friction in Vacuum

An increase in the surface temperature of a-C:H films tends to cause chemical changes, as discussed in the preceding subsection. These chemical changes can alter their friction and wear behavior. For simplicity of discussion, the effect of temperature on tribological properties of concern is investigated in a nonoxidizing environment (i.e., in an ultrahigh vacuum). The in situ friction experiments were conducted in a vacuum with the as-received plasma-deposited a-C:H films in contact with the ion-sputter-cleaned, hemispherical monolithic  $\text{Si}_3\text{N}_4$  rider specimens.

Typical plots of the coefficient of friction for a-C:H films plasma-deposited at 150 and 300 W as a function of surface temperature are presented in figures 11(a) and (b), respectively. Comparative data for an uncoated  $\text{Si}_3\text{N}_4$  flat in contact with a hemispherical  $\text{Si}_3\text{N}_4$  rider are presented in figure 12.

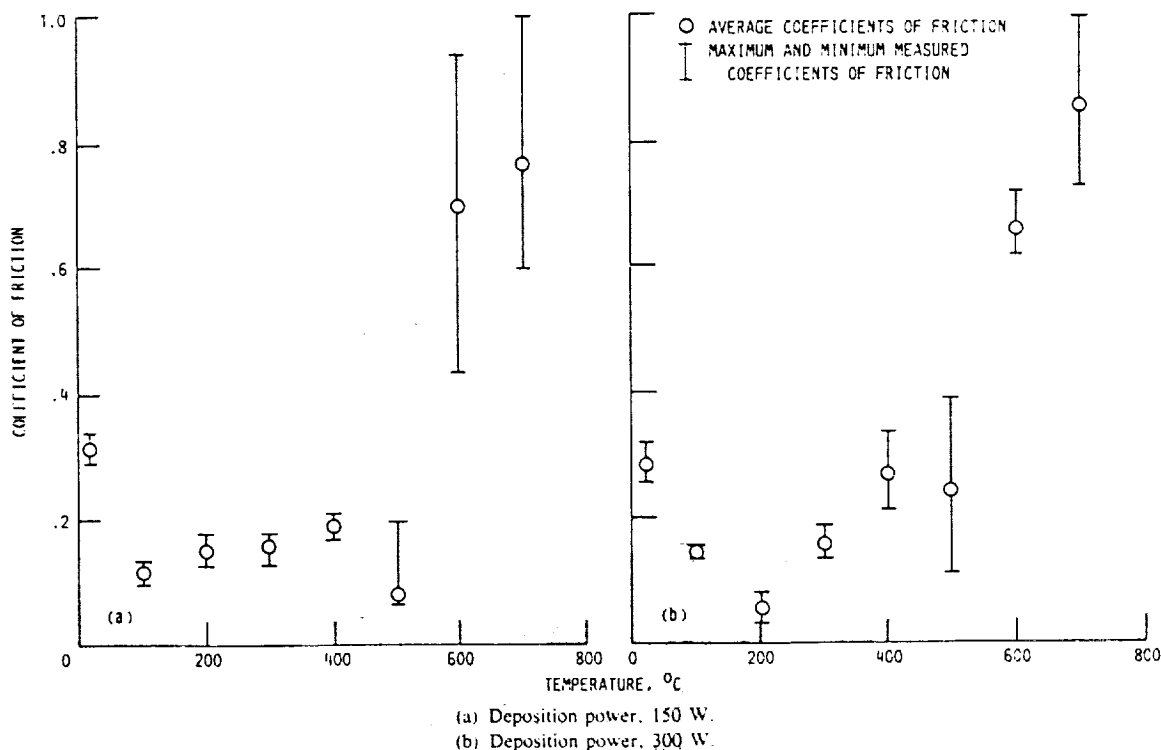


Figure 11.—Coefficients of dynamic friction as function of temperature for a-C:H films in contact with  $\text{Si}_3\text{N}_4$  rider specimens in vacuum.

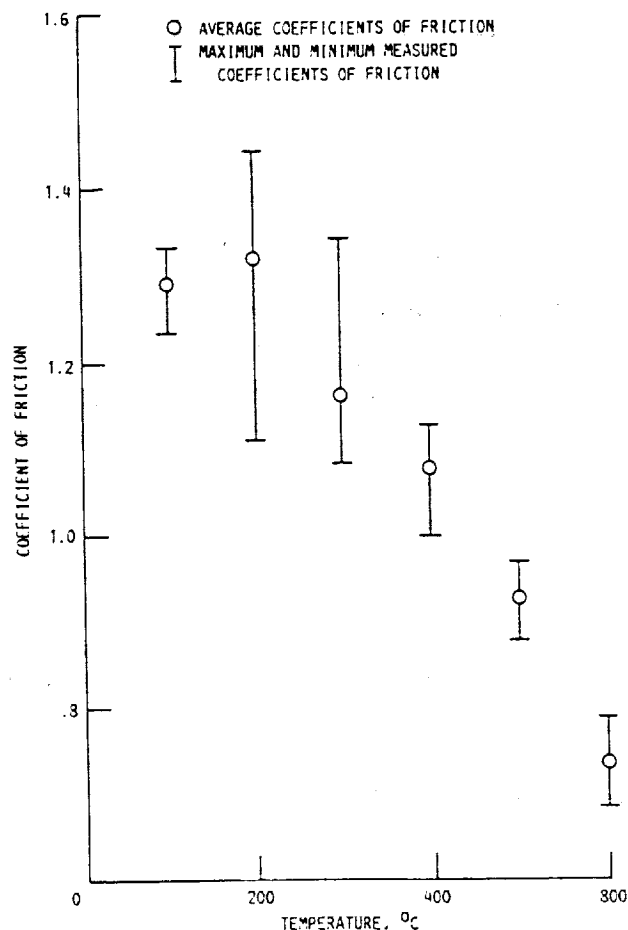


Figure 12.—Coefficients of dynamic friction as function of temperature for  $\text{Si}_3\text{N}_4$  flats in contact with  $\text{Si}_3\text{N}_4$  rider specimens in vacuum.

With the 150- and 300-W plasma-deposited a-C:H films (fig. 11), the coefficient of friction remained low at temperatures to 500 °C and rapidly increased with increasing temperatures at 600 °C and above, remaining high in the range of 600 to 700 °C. The mechanism involved in the rapid increase in friction at 600 to 700 °C should be related to the two-step process, namely carbonization and polymerization of a-C:H films, as discussed in the preceding subsection.

When compared with the coefficient of friction for  $\text{Si}_3\text{N}_4$  in contact with  $\text{Si}_3\text{N}_4$  itself (fig. 12), the coefficient of friction for a-C:H films in contact with a  $\text{Si}_3\text{N}_4$  rider (fig. 11) was generally much lower at temperatures to 500 °C. It is also interesting to note that the coefficient of friction for the film deposited at 150 W had a very low coefficient of friction (about 0.08 at 500 °C) even in an ultrahigh vacuum environment (fig. 11(a)), and that the film effectively lubricated  $\text{Si}_3\text{N}_4$  surfaces. Note that in vacuum the friction behavior of a-C:H film deposited at 50 W was similar to that shown in figure 11(a).

### CONCLUDING REMARKS

There are two parts in this chapter, one mainly describing the growth and physical characterization of a-C:H films and the other dealing with the tribological properties. The films can be characterized by several parameters, as described in the first part. The main properties are defined by bonding ratios ( $sp^2/sp^3$ ) and by hydrogen concentration, which will give the graphitic or diamondlike behavior. The more graphitic behavior is associated with lower bandgap and low mechanical etch rate.

In the second part of the work, the a-C:H films were shown to be capable of tribological applications. Plasma-deposited a-C:H can be effectively used as hard, wear-resistant, and protective lubricating films on ceramic material under a variety of environmental conditions such as moist air, dry nitrogen, and vacuum. More specifically, we

found a very good correlation of the tribological behavior with the physical properties, as described in the first part of the work. For a-C:H films deposited at low power, which are more diamondlike, we found friction behavior similar to that of bulk diamond. The present experiments show that among the a-C:H films deposited at various deposition powers (50 to 300 W), the film deposited at 50 W had the lowest initial coefficient of friction in dry nitrogen. The value of the coefficient of friction (0.08 to 0.09) was similar to that of hemispherical diamond (radius, 0.2 mm) in sliding contact with a Si<sub>3</sub>N<sub>4</sub> flat. Conversely, for the a-C:H films deposited at higher power, a graphitic tribological behavior was found. Effective lubrication is possible with the graphitic films like bulk graphite when adsorbed water vapor is present.

Lastly, a simple physical characterization of the films can partially predict the tribological properties.

## REFERENCES

1. Angus, J.J., Koidl, P., and Domitz, S.: "Carbon Thin Films," in *Plasma Deposited Thin Films*, ed. by Mort, J. and Jansen, F. CRC Press Inc., 1986, pp. 89-127.
2. Aisenberg, S., and Chabot, R.: *J. Appl. Phys.*, 1971, **42**, 2953.
3. Holland, L., and Ojha, S.M.: *Thin Solid Films*, 1978, **48**, L21.
4. Berg, S., and Andersson, L.P.: *Thin Solid Films*, 1979, **58**, 117.
5. Meyerson, B., and Smith, F.W.: *Solid State Commun.*, 1980, **34**, 531.
6. Moravec, T.J., and Orent, T.W.: *J. Vac. Sci. Technol.*, 1981, **18**, 226.
7. Vora, H., and Moravec, T.J.: *J. Appl. Phys.*, 1981, **52**, 6151.
8. Banks, B.A., and Rutledge, S.K.: *J. Vac. Sci. Technol.*, 1982, **21**, 807.
9. Khan, A.A., Woollam, J.A., Chung, Y., and Banks, B.A.: *IEEE Electron Devices Lett.*, 1983, **4**, 146.
10. Khan, A.A., Woollam, J.A., and Chung, Y.: *Solid-State Electron.*, 1984, **27**, 385.
11. Kikuchi, M., Hikita, M., and Tamamura, T.: *Appl. Phys. Lett.*, 1986, **48**, 835.
12. Pouch, J.J., Warner, J.D., Liu, D.C., and Alterovitz, S.A.: *Thin Solid Films*, 1988, **157**, 97.
13. Warner, J.D., Pouch, J.J., Alterovitz, S.A., Liu, D.C., and Lanford, W.A.: *J. Vac. Sci. Technol. A*, 1985, **3**, 900.
14. Alterovitz, S.A., Pouch, J.J., and Warner, J.D.: "Rapid Thermal Annealing of Amorphous Hydrogenated Carbon (a-C-H) Films," in *Rapid Thermal Processing of Electronic Materials*, MRS Symp. Proc. Vol. 92, ed. by Wilson, S.R., Powell, R., and Davies, D.E., Materials Research Society, 1987, pp. 311-318.
15. Pouch, J.J., Warner, J.D., and Liu, D.C.: *Carbon Films Grown from Plasma on III-V Semiconductors*, NASA TM-87140, 1985.
16. Pouch, J.J., Alterovitz, S.A., Warner, J.D., Liu, D.C., and Lanford, W.A.: "Optical Properties of Hydrogenated Amorphous Carbon Films Grown from Methane Plasma," in *Thin Films: The Relationship of Structure to Properties*, MRS Symp. Proc. Vol. 47, ed. by Aita, C.R. and Sreeharsha, K.S., Materials Research Society, 1985, pp. 201-204 (Also, NASA TM-86995).
17. Alterovitz, S.A., Warner, J.D., Liu, D.C., and Pouch, J.J.: "Ellipsometric and Optical Study of Some Uncommon Insulator Films on III-V Semiconductors," in *Dielectric Films on Compound Semiconductors*, Electrochemical Society Symp. Proc. Vol. 86-3, ed. by Kapoor, V.J., Connolly, D.J., and Wong, Y.H., The Electrochemical Society, Pennington, NJ, 1986, pp. 59-77 (Also, NASA TM-87135).
18. Pouch, J.J., Alterovitz, S.A., and Warner, J.D.: "Optical and Compositional Properties of a-C:H and BN Films," in *Plasma Processing*, MRS Symp. Proc. Vol. 68, ed. by Coburn, J.W., Gottscho, R.A., and Hess, D.W., Materials Research Society, 1986, pp. 211-216 (Also, NASA TM-87258).
19. Benninghoven, A.: *Surf. Sci.*, 1975, **53**, 596.
20. Wagner, J., Wild, Ch., Pohl, F., and Koidl, P.: *Appl. Phys. Lett.*, 1986, **48**, 106.
21. Kobayashi, K., Mutsukura, N., and Machi, Y.: *J. Appl. Phys.*, 1986, **59**, 910.
22. Kaplan, S., Jansen, F., and Machonkin, M.: *Appl. Phys. Lett.*, 1985, **47**, 750.
23. Miyoshi, K., and Rengstorff, G.W.P.: *Corrosion*, 1989, **45**, 266.
24. Miyoshi, K., and Buckley, D.H.: *Wear*, 1986, **110**, 295.
25. Miyoshi, K., Pouch, J.J., Alterovitz, S.A., Pantic, D.M., and Johnson, G.A.: in *Wear of Materials*, Vol. 2, ed. by Ludema, K.C., ASME, 1989, p. 585.
26. Enke, K., Dimigen, H., and Hubsch, J.: *Appl. Phys. Lett.*, 1980, **36**, 291.
27. Memming, R.: *Thin Solid Films*, 1986, **143**, 279.
28. Okada, K., and Namba, Y.: *J. Vac. Sci. Technol. A*, 1989, **7**, 132.
29. Bowden, F.P., and Tabor, D.: "The Friction and Lubrication of Solids—Part II," Clarendon Press, Oxford, 1964, pp. 158-185.
30. Praver, S., Kalish, R., and Adel, M.: *Appl. Phys. Lett.*, 1986, **48**, 1585.
31. Robertson, J.: *Adv. Phys.*, 1986, **35**, 317.
32. Bisson, E.E.: "Nonconventional Lubricants," in *Advanced Bearing Technology*, ed. by Bisson, E.E. and Anderson, W.J., NASA SP-38, 1965, pp. 203-258.
33. Bisson, E.E., Johnson, R.L., and Anderson, W.J.: "Friction and Lubrication with Solid Lubricants at Temperatures to 1000 °F with Particular Reference to Graphite," in *Proceedings of the Conference on Lubrication and Wear*, Institution of Mechanical Engineers, London, England, 1957, pp. 348-354.

# Characterization of Multilayer GaAs/AlGaAs Transistor Structures by Variable Angle Spectroscopic Ellipsometry

Kenneth G. MERKEL\*, Paul G. SNYDER, John A. WOOLLAM,  
Samuel A. ALTEROVITZ\*\* and A. K. RAI\*\*\*

Department of Electrical Engineering, Center for Microelectronic and Optical Materials Research,  
University of Nebraska-Lincoln, Lincoln, Nebraska 68588-0511, USA

(Received January 7, 1989; accepted for publication March 25, 1989)

Variable angle of incidence spectroscopic ellipsometry (VASE) has been implemented as a means of determining layer thickness, alloy composition, and growth quality of GaAs/AlGaAs samples composed of relatively thick layers as well as superlattices. The structures studied in this work contained GaAs/AlGaAs multilayers with a superlattice "barrier" and were grown for later formation of modulation-doped field effect transistors (MODFETs). Sample modeling was performed by treating the superlattice as a bulk AlGaAs layer of unknown composition. Extremely good data fits were realized when five layer thicknesses and two alloy ratios were allowed to vary in a regression analysis. Room temperature excitonic effects associated with the e-hh(1), e-lh(1) and e-hh(2) transitions were observed in the VASE data.

**KEYWORDS:** ellipsometry, spectroscopic, variable angle, layer thicknesses, GaAs, AlGaAs multilayer transistors

## §1. Introduction

Rapid progress has occurred in the development of modulation-doped and multiple quantum well heterostructure devices. These types of structures have found applications in opto-electronics, digital electronics and microwave analog communications.<sup>1)</sup>

These advances have created a requirement for monitoring the accuracy and quality of III-V semiconductor growth processes. Traditional methods for these purposes include cross sectional TEM (XTEM) and photoluminescence.<sup>2,3)</sup> XTEM is slow, expensive, and destructive, and photoluminescence (PL) does not yield thickness information for the thicker layers. Generally PL, as well as photomodulation measurements, must be performed at cryogenic temperatures to be maximally useful. This limits the usefulness of these techniques in a manufacturing environment. VASE has been shown to provide an accurate, room temperature, atmospheric pressure, and nondestructive method of characterizing samples containing heterojunction and superlattice layers.<sup>4,5,6)</sup> Thus it is logical to extend application of VASE to the more complex structure represented in the present paper. Important additional considerations such as interfacial roughness,<sup>7)</sup> wafer homogeneity, and oxide growth can be determined by the VASE process.<sup>8,9)</sup> In the present work we determine five layer thicknesses and two (equivalent) alloy ratios, representing one of the more complicated structures yet analyzed by ellipsometry. With these many unknowns the full spectral and variable angle capabilities of the VASE technique are required. Because we are "pushing the technique to the limit," we have included a careful study of the mean square error and correlation, in the present work.

Optical switches and modulators require very large nonlinearities induced optically or electro-optically. These nonlinearities are inherent in excitonic resonances in bulk semiconductors at low temperatures. The observance of excitonic effects in superlattices at room temperature greatly enhances the suitability of their use with other opto-electronic devices.<sup>10)</sup> VASE provides important information for these devices, specifically the index of refraction and extinction coefficient at excitonic transition energies in superlattices.<sup>6)</sup>

VASE resolves the structural and dielectric properties of multilayered samples by measuring the ratio of the reflection coefficients for light polarized parallel ( $R_p$ ), and perpendicular ( $R_s$ ) to the plane of incidence.<sup>11)</sup> The ellipsometric parameters can be expressed as

$$\rho = \tan \Psi \exp(i\Delta) = R_p/R_s \quad (1)$$

Experimentally,  $\Psi$  and  $\Delta$  are measured and results are compared in a regression analysis to  $\Psi'$  and  $\Delta'$  which are calculated using the Fresnel reflection coefficients and effective medium theories. The results of this analysis are values for layer thicknesses, alloy compositions and optical constants as a function of wavelength. In the present paper we use VASE to obtain layer thicknesses and alloy fractions for MODFET structures containing superlattices.

In §2 the experimental set-up is discussed. Section 3 details the VASE modeling procedure. Results are presented in §4 and conclusions in §5.

## §2. Experiment

The design of the ellipsometric measuring system used for the present experiment is based upon a design by Aspnes and Studna.<sup>12)</sup> The basic ellipsometer is a Gaertner model L119 with the additional capability of setting the angle of incidence,  $\phi$ , over a wide range of values from 20° to almost 90° with an accuracy of  $\pm 0.01^\circ$ . The analyzer rotates at an angular speed of 3600 rpm, and a 75 W Xenon short arc lamp is used as a light source. The

\*AFWAL/ELRA, Electronics Technology Laboratory, Wright-Patterson AFB, OH 45433-6543

\*\*NASA Lewis Research Center, Cleveland, Ohio 44135

\*\*\*Universal Energy Systems, 4401 Dayton-Xenia Road, Dayton, Ohio 45432

400, 300 Å GaAs
325 Å Al <sub>0.3</sub> Ga <sub>0.7</sub> As
SI Planar Layer 6E12 cm <sup>-2</sup>
75 Å Al <sub>0.3</sub> Ga <sub>0.7</sub> As
150 Å GaAs
200 Å Al <sub>0.3</sub> Ga <sub>0.7</sub> As
20, 30 Å GaAs
GaAs Substrate

} 25/24 Periods

Fig. 1. Superlattice structure for samples #2352, #2207.

output of the arc lamp is passed through a Kratos GM252 monochromator providing a 2500–8500 Å spectral range with a typical linewidth of 20 Å. The narrow light beam from the monochromator output passes through a polarizer to the sample where it is reflected through a rotating analyzer. A photomultiplier tube (PMT) measures the intensity of the light beam at the output of the analyzer. The PMT output is digitized and collected by a computerized data acquisition system, from which  $\Psi$  and  $\Delta$  are calculated using a Fourier analysis.

The sensitivity of ellipsometric measurements is a strong function of  $\phi$  with maximum sensitivity occurring at the wavelength-dependent, principal (pseudo-Brewster) angle.<sup>11,13</sup> The principal angle can be estimated prior to measurement by modeling the assumed structure for the sample and generating three-dimensional plots of  $\Psi$  or  $\Delta$  vs. wavelength and  $\phi$ . VASE allows measurement at several angles close to the principal angle, as opposed to spectroscopic ellipsometry (SE), in which measurements are made at a fixed, single value of  $\phi$ . For the two samples used in this study, measurements were made at  $\phi = 75.5^\circ$  and  $76.5^\circ$  (for sample #2207), and at  $\phi = 76^\circ$  (for sample #2352) which are very near the principal angles over most of the spectral range. The data for these experiments were taken in the 3500 to 8000 Å spectral range in increments of 25 Å.

The nominal structure of the two measured samples is shown in Fig. 1. The layers were grown by molecular beam epitaxy in a Varian II machine on an undoped liquid encapsulated Czochralski (LEC) GaAs substrate.<sup>13</sup> The substrate was rotated at 7 rpm during deposition with the deposition rates and the Al to Ga ratio calibrated using RHEED intensity oscillations.<sup>9</sup> The superlattice buffer provides a high quality barrier at the quantum well/superlattice interface. The superlattice GaAs wells are nominally 20 Å thick for sample #2207 and 30 Å thick for sample #2352. The 75 Å AlGaAs section is an undoped spacer layer which separates mobile carriers within the 150 Å GaAs well from ionized impurities in the 325 Å doped AlGaAs layer. A single atomic plane of Si provides "delta" doping for the quantum well, and the 400 Å GaAs layer at the top is used as a surface cap.

### §3. Modeling

The model used to analyze the VASE data is shown in Fig. 2(a). The optical constants of bulk materials are nor-

25 Å Oxide
400 Å GaAs
400 Å Al <sub>0.3</sub> Ga <sub>0.7</sub> As
150 Å GaAs
5500 Å Al <sub>0.3</sub> Ga <sub>0.7</sub> As
GaAs Substrate

(a)

25.88 Å Oxide
437 Å GaAs
405 Å Al <sub>0.37</sub> Ga <sub>0.63</sub> As
141 Å GaAs
5115 Å Al <sub>0.32</sub> Ga <sub>0.68</sub> As
GaAs Substrate

(b)

Fig. 2. a) VASE model, and b) fical model for sample #2352.

mally used for the modeling procedure. However, in superlattices the quantum energy subbands, along with the added complexity of wave function overlap, nullifies the use of bulk material properties.<sup>15</sup> Because the optical constants of real superlattices are not independently known, the superlattice was modeled as a single Al<sub>x</sub>Ga<sub>1-x</sub>As layer of unknown thickness and composition. A native oxide layer was also incorporated into the model on top of the GaAs cap. Optical constants of Al<sub>x</sub>Ga<sub>1-x</sub>As and GaAs were kindly provided by Dr. David Aspnes of Bellcore, Inc., USA.

The thicknesses and compositions of the superlattice "equivalent layer" as well as the other layers were solved for in a regression analysis. A Fortran program produces calculated  $\Psi$  and  $\Delta$  values using the model, then minimizes the mean-square (MSE) between the measured and calculated ellipsometric error parameters by using the Marquardt minimization algorithm.<sup>16,17</sup> The MSE is expressed as

$$MSE = 1/m \sum_i \{(\Psi_c - \Psi_e)^2 + (\Delta_c - \Delta_e)^2\}^{1/2} \quad (2)$$

where the subscripts c and e represent the calculated and experimental values respectively and m is the number of measurements. Occasionally the minimization is done with respect to  $\Psi$  only, due to the adverse effects on delta values if there is a change in the sense of polarization handedness.

### §4. Results

In order to obtain the best possible fits to the experimental data, a number of modeling approaches were utilized. The results of the modeling sequence for both samples are shown in Table I. The initial best fit was over the entire (3500 to 8000 Å) spectral range where the MSE was minimized for both  $\Psi$  and  $\Delta$ . Due to the shorter wavelength light being absorbed closer to the surface, the

Table I. Results of VASE and XTEM Analyses (all thicknesses and wavelengths in Å).

Sample: #2352								
	t1	t2	t3	x3	t4	t5	x5	MSE
Nominal values	25	400	400	0.30	150	5,500	0.30	—
VASE	26	435	413	0.37	142	5,470	0.32	0.069
90% confidence limits ( $\pm$ )	1	8	16	0.005	10	20	0.001	—
XTEM	460*		420	—	160	5,420	—	—
* combined thickness of layers t1 and t2								
Sample: #2207								
	t1	t2	t3	x3	t4	t5	x5	MSE
Nominal values	25	300	400	0.30	150	5,520	0.30	—
VASE	25	286	275	0.35	153	5,115	0.21	0.076
90% confidence limits ( $\pm$ )	2	10	24	0.01	18	37	0.01	—

analysis range was decreased to 3500–6800 Å in order to focus on the layers above the superlattice. Results from the 3500–6800 Å analysis were used as input parameters for a  $\Psi$  only data analysis over the full spectral range. This ensured that the fitting procedure would be more sensitive to the superlattice parameters. The final model for sample #2352 with corresponding layer thicknesses, composition and MSE is shown in Fig. 2(b). These values are from the  $\Psi$  only type data fits shown in Table I. The 90% confidence limits for the final model are also exhibited.

An additional analysis of sample #2352 was conducted using XTEM. The XTEM results (Table I) are in good agreement with those of VASE and serve to verify the accuracy of the VASE layer thickness measurements. The XTEM photographs showed that the material layers were uniform with abrupt interfaces. A previous study<sup>18)</sup> of a less complicated GaAs/AlGaAs system has also demonstrated the concurrence between XTEM and VASE layer thickness determinations.

Of particular importance in the VASE data analysis procedure is ensuring that the MSE (defined by eq. 2) obtained from a set of starting values is the true minimum MSE and not a satellite minimum (defined as a local minimum, but not the lowest minimum). Therefore, the MSE for a variety of starting values were analyzed. The variation of MSE with respect to changes in each particular model variable, keeping all other variables fixed, was obtained for sample #2352. Figure 3 shows changes in MSE for the alloy composition variations as each composition is fixed at a series of values centered near its optimum solved value, and the other composition is fixed at its best fit value. The MSE is presented with respect to the 90% confidence limits of Table I added to or subtracted from the VASE "best" solution values. The 90% confidence limit is a statistical measure of the uncertainty of a particular measured parameter. Values for the present experiments are given in Table I. It is evident from the figure that the starting value for a single variable analysis could deviate from the solved value by a factor of approximately 15 times the 90% con-

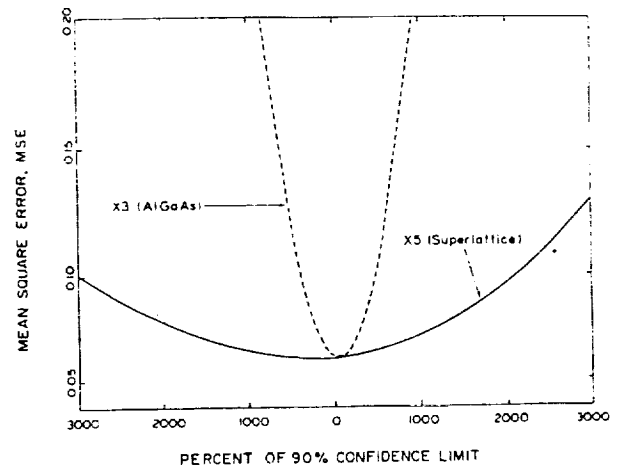


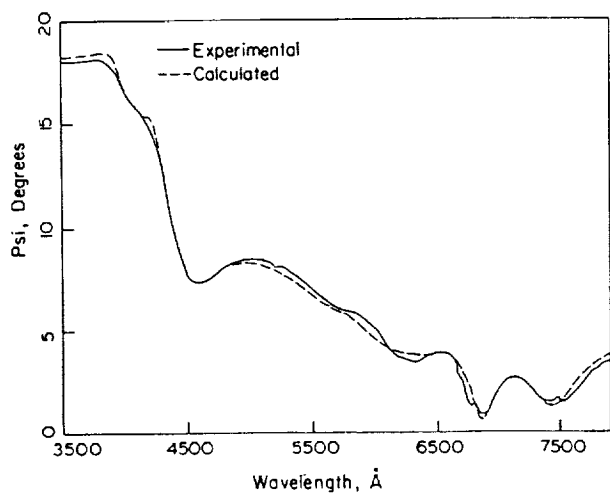
Fig. 3. Mean square error vs. percent of 90% confidence limit added to VASE solution value for the alloy compositions of sample #2352.

fidence limit and the best fit MSE would still be realized in the regression analysis. The figure also demonstrates that the 90% confidence limits applied to the VASE solutions lie well within the region for a correct minimum.

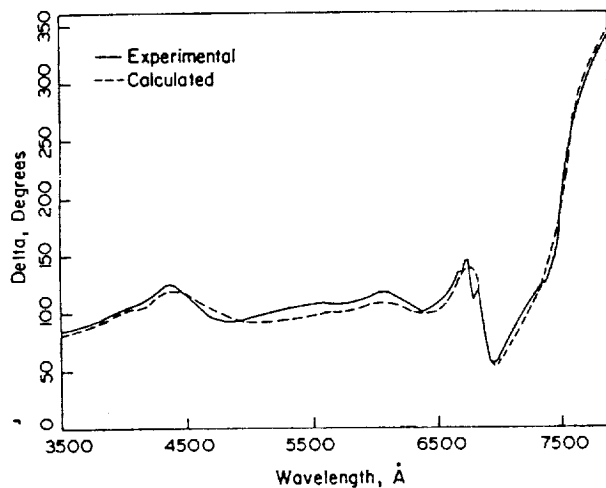
Plots of the experimental and calculated VASE data for sample #2352 are shown in Figs. 4(a) and 4(b), and for sample #2207 in Figs. 5(a) and 5(b). A good fit of the calculated data to the general features of the experimental data was obtained. The data are matched particularly well considering that there are seven variables with varying degrees of correlation between them. The good data fits are evidence that replacing the superlattice with an "effective"  $\text{Al}_x\text{Ga}_{1-x}\text{As}$  layer is a reasonable approach for this specific case, where the AlGaAs barriers are thick when compared to the GaAs quantum well thicknesses.

The broad peaks in the  $\Psi$  data at 5800, 6500, 7200 and 7900 Å for #2352, and 6000, 6800, and 7500 Å for #2207 are mainly the result of optical interference effects from the superlattice region. Spectral features at the shorter wavelengths are dominated by the top layer of GaAs. However, the spectral details at all wavelengths are influenced to some degree by each of the layers; in particular the surface oxide. This is shown by Figs. 6 through 9 which are discussed below.

Figures 6 through 9 were made by fixing the thickness and composition values found from the analysis of sample #2352 and sequentially varying one parameter at a time for a single  $\phi$ . Figures 6 and 7 exhibit how the superlattice effects spectra in the 6000 to 8000 Å range. It is apparent from Fig. 6 that increasing the superlattice thickness causes a corresponding increase in the amplitude and a shift to higher wavelengths of the  $\Psi$  spectra. However, an increase in the value of superlattice composition is seen to cause an increase in amplitude and decrease in the wavelength shift (Fig. 7). Variation of the thickness of the upper layer of GaAs has a pronounced effect in  $\Psi$  between 4400 and 5200 Å (Fig. 8), and also causes leveling between maxima and minima at higher wavelengths. Changing the oxide thickness uniformly shifts the amplitude of  $\Psi$  over the entire wavelength



(a)

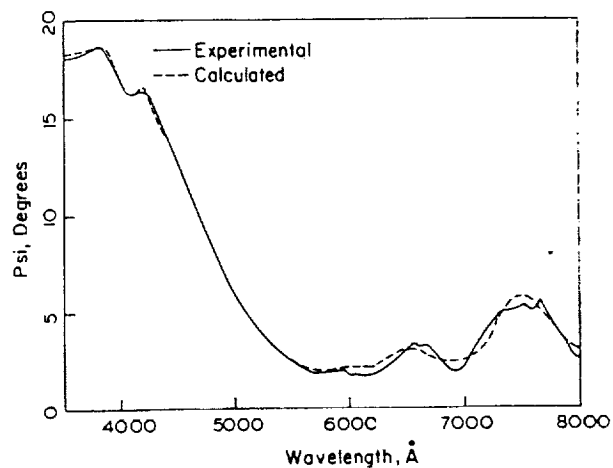


(b)

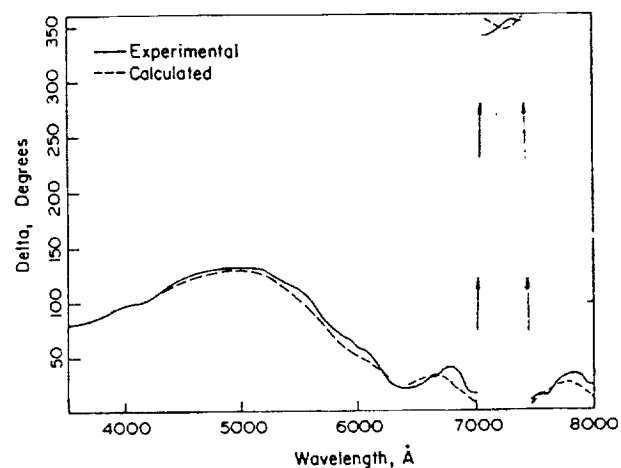
Fig. 4. a) Psi, and b) delta vs. wavelength for sample #2352.

range (Fig. 9).

The growth quality of the superlattice was determined prior to the XTEM analysis by studying interfacial smoothness between layers. In order to appraise roughness, a Bruggeman effective medium approximation was performed on sample #2352 with a 20 Å mixture of GaAs and  $\text{Al}_{0.3}\text{Ga}_{0.7}\text{As}$  in the model between the 150 Å GaAs layer and the superlattice. The solution showed no appreciable change in values for layer thickness of composition. This resulted in an increase in the MSE of only 0.3%, demonstrating that physically there is not a mixture (roughness) layer present. Another modeling trial incorporated an  $\text{Al}_2\text{O}_3$  layer in between the same layers. This analysis was done to determine if roughness existed due to the burial of oxygen impurities (which are Al composition dependent) in the GaAs portion of the GaAs/AlGaAs interface.<sup>19)</sup> The oxide layer solved to less than 2 Å with no change in MSE. Thus VASE in addition to XTEM has shown that the superlattice growth quality



(a)



(b)

Fig. 5. a) Psi, and b) delta vs. wavelength for sample #2207.

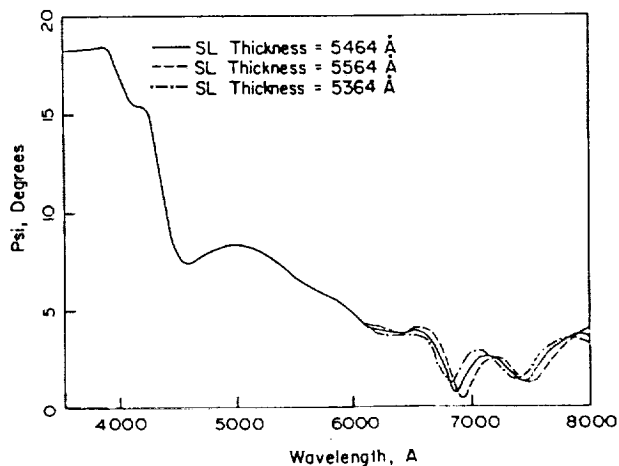


Fig. 6. Generated psi vs. wavelength for sample #2352 with varying superlattice thickness.

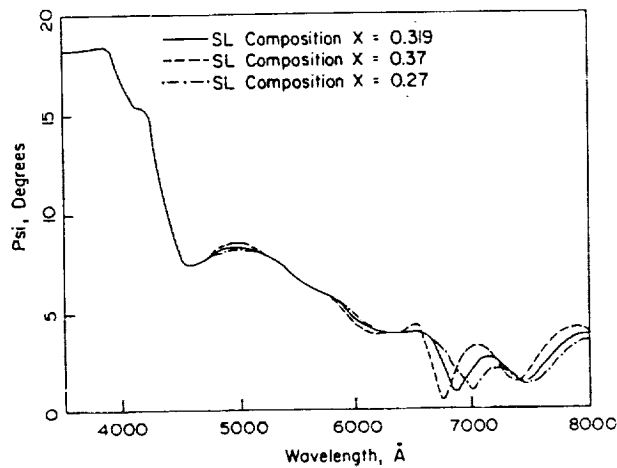


Fig. 7. Generated psi vs. wavelength for sample #2352 with varying superlattice composition.

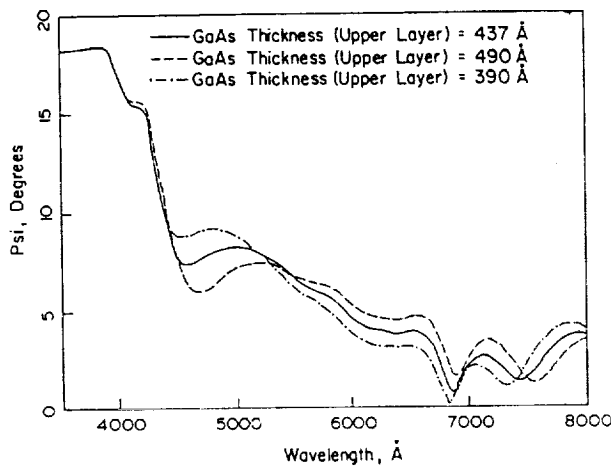


Fig. 8. Generated psi vs. wavelength for sample #2352 with varying thickness of upper GaAs layer.

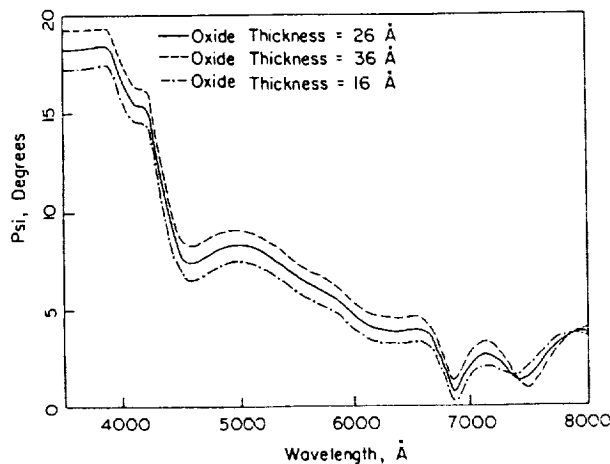


Fig. 9. Generated psi vs. wavelength for sample #2352 with varying surface oxide thickness.

is good since incorporation of a GaAs/AlGaAs mixture or oxide into the regression analysis worsened the fits.

The narrow excitonic structures seen in Fig. 5(a) at 6530 Å, 7500 Å, and 7700 Å, are respectively the second electron to heavy hole, e-hh(2), first electron to light hole, e-lh(1), and first electron to heavy hole, e-hh(1), transitions in the superlattice quantum wells. The exciton energies are in qualitative agreement with values predicted by subtracting the exciton binding energy (9.1 meV in single quantum well GaAs) from the e-hh(1) transition energy of a quantum well with a 30 Å well width and a wide  $\text{Al}_{0.3}\text{Ga}_{0.7}$  barrier.<sup>20</sup> This analysis yields:  $E_{e-hh(1)} = 1.582$  (7,840 Å). This approach is sufficient due to the barrier width being large in comparison to the well width. It follows that the e-lh(1) and e-hh(2) transitions are the next sharp structure when moving toward higher energies.

The exciton peaks are shown in Fig. 10 for sample #2207 measured at 10 Å intervals. The presence of the excitonic structure in both samples confirms that the superlattice interfaces are of good quality. The broadness of the excitonic structure can most likely be attributed to slight energy changes in the quantum levels associated with layer thickness variations in the GaAs layers of the superlattice. Also, thermal broadening of approximately 100 Å is a factor at room temperature measurements. The exciton lines from levels in the 150 Å quantum well are outside of the spectral range shown.

## §5. Conclusion

We have found that the superlattices in MODFET/superlattice structures can be effectively incorporated in the VASE modeling sequence by representing the superlattice as a bulk AlGaAs layer of unknown alloy composition. In the future it would be beneficial to make independent measurements of the optical constants of superlattices. This would be an enormous task since each superlattice design would have unique optical properties. Modeling the superlattice as multilayers, each having the bulk GaAs and AlGaAs optical properties, gives poor results. Thus the approach we have taken works

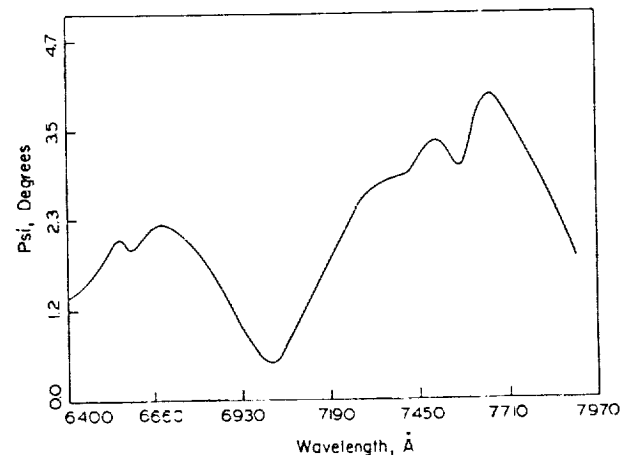


Fig. 10. Excitonic spectra for sample #2207.

reasonably well, and is applicable to any superlattice structure.

Analysis of five layers and two alloy fractions is possible if data are taken near the wavelength dependent pseudo-Brewster angle. Room temperature excitonic effects as well as growth quality determination are realized using the VASE measurement process. Thus the analysis of these structures through VASE can provide an accurate and nondestructive assistance in the production of semiconductor structures for optoelectronic and microwave communication devices.

#### Acknowledgements

This research was supported by NASA Lewis Research Center grant NAG3-154. The authors would like to thank D. C. Radulescu and L. F. Eastman of Cornell University for providing the samples.

We would also like to thank Dr. David Aspnes for supplying accurate values for the optical dielectric response function vs. photon energy for GaAs and  $Al_xGa_{1-x}As$ .

#### References

- 1) T. J. Drummond, W. T. Masselink and H. Morkoc: Proc. IEEE **74** (1986) 773.
- 2) O. J. Glembocki, F. H. Pollak and J. J. Song: Proc. of SPIE Vol. 794, see especially invited paper by K. K. Bajaj and D. C. Reynolds on p.2 (1987).
- 3) Mater. Res. Soc. Symp. Proc. **77** (1987) 755.
- 4) P. G. Snyder, J. E. Oh, J. A. Woollam and R. E. Owens: Appl. Phys. Lett. **51** (1987) 770.
- 5) P. G. Snyder, J. E. Oh and J. A. Woollam: Mater. Res. Soc. Proc. **77** (1987) 761.
- 6) P. G. Snyder, B. N. De, K. G. Merkel, J. A. Woollam, D. W. Langer, C. E. Stutz, R. Jones, A. K. Rai and K. Evans: Superlattices & Microstructures **4** (1988) No. 1, 97.
- 7) M. Erman, J. B. Theeten, N. Vodjdani and Y. Demay: J. Vac. Sci. & Technol. **B1** (1983) 328.
- 8) S. A. Alterovitz, P. G. Snyder, K. G. Merkel, J. A. Woollam, D. C. Radulescu and L. F. Eastman: J. Appl. Phys. **63** (1988) 5081.
- 9) H. Burkhard, H. W. Dinges and E. Kuphal: J. Appl. Phys. **53** (1982) 655.
- 10) D.S. Chemla: Proc. of Basic Properties of Optical Materials, ed. A. Feldman (NBS Publication 697, 1985) p. 202.
- 11) R. M. A. Azzam and N.M. Bashara: *Ellipsometry and Polarized Light* (North-Holland Publishing, New York, N.Y., 1977).
- 12) D. E. Aspnes and A. A. Studna: Appl. Opt. **14** (1975) 220.
- 13) P. G. Snyder, M. C. Rost, G. H. Bu-Abbud, J. A. Woollam and S. A. Alterovitz: J. Appl. Phys. **60** (1986) 3293.
- 14) D. C. Radulescu, G. W. Wicks, W. J. Schaff, A. R. Calawa and L. F. Eastman: J. Appl. Phys. **62** (1987) 954.
- 15) J. N. Schulman and Y. C. Chang: Phys. Rev. **B31** (1985) 2056.
- 16) D. W. Marquardt: J. Soc. Indus. Appl. Math. **11** (1963) 431.
- 17) G. H. Bu-Abbud, N. M. Bashara and J. A. Woollam: Thin Solid Films **138** (1986) 27.
- 18) J. A. Woollam, P. G. Snyder, A. W. McCormick, A. K. Rai, D. C. Ingram, P. P. Pronko and J. J. Geddes: Mater. Res. Soc. Symp. Proc. **77** (1987) 755.
- 19) T. Achtwich, G. Burri, M. A. Py and M. Ileyems: Appl. Phys. Lett. **50** (1987) 1730.
- 20) R. L. Greene and K. K. Bajaj: Solid State Commun. **45** (1983) 831.